

# Skyrmion Phase in MnSi Thin Films Grown on Sapphire by a Conventional Sputtering

**Won-Young Choi**

Sogang University

**Hyun-Woo Bang**

Sogang University

**Seung-Hyun Chun**

Sejong University

**Sunghun Lee** (✉ [kshlee@sejong.ac.kr](mailto:kshlee@sejong.ac.kr))

Department of Physics, Sejong University, Seoul 05006, Korea <https://orcid.org/0000-0002-1974-8110>

**Myung-Hwa Jung**

Sogang University

---

## Nano Express

**Keywords:** MnSi, Sputtering, Polycrystal, Skyrmion, Topological Hall effect

**Posted Date:** October 30th, 2020

**DOI:** <https://doi.org/10.21203/rs.3.rs-97855/v1>

**License:**  This work is licensed under a Creative Commons Attribution 4.0 International License.

[Read Full License](#)

---

**Version of Record:** A version of this preprint was published on January 6th, 2021. See the published version at <https://doi.org/10.1186/s11671-020-03462-2>.

# Abstract

Topologically protected chiral skyrmion is an intriguing spin texture, which has attracted much attention because of fundamental research and future spintronic applications. MnSi with the non-centrosymmetric structure is well-known material hosting skyrmion phase. To date, preparation of MnSi crystals has been investigated by using special instruments with ultrahigh vacuum chamber. Here, we introduce a facile way to grow MnSi films on sapphire substrate using a relatively low vacuum environment of conventional magnetron sputtering. Although as-grown MnSi films have polycrystalline nature, the stable skyrmion phase in a broad range of temperatures and magnetic fields is observed by magnetotransport properties including phenomenological scaling analysis of Hall resistivities contribution. Our findings provide not only a general way to prepare the materials possessing skyrmion phase, but also insight into further research to stimulate more degrees of freedom in our inquisitiveness.

## Introduction

Topologically protected chiral skyrmion is a vortex-like nontrivial swirling spin texture, where magnetic spins stabilized by Dzyaloshinskii-Moriya interaction (DMI) align in non-collinear manner surrounding a sphere.<sup>1</sup> Large DMI is generally induced in non-centrosymmetric ferromagnets, owing to broken inversion symmetry.<sup>2</sup> This complex spin texture has garnered massive attention because of intriguing physical properties for both fundamental research and possible applications in future technology.<sup>3,4</sup> Compared to magnetic domain walls, skyrmion domains exhibit stable current-driven motion at remarkably low current density, enabling low-power consumption spintronic devices.<sup>5</sup>

MnSi with the non-centrosymmetric B20 phase is an archetypal helimagnetic material hosting skyrmionic lattice, which has been studied theoretically and experimentally for decades.<sup>6-10</sup> In the skyrmionic lattice of MnSi, the spin transfer torque (STT) is observed, leading to further investigations on the injection of spin-polarized currents.<sup>5</sup> In especial, the skyrmion size of MnSi is ranged in  $\sim 18$  nm, considered small among well-known groups with skyrmion spin texture.<sup>11</sup> STT tends to increase significantly with reducing the skyrmion size.<sup>12,13</sup> Although material parameters affect the skyrmion size, DMI and ferromagnetic exchange interaction mainly contribute to determine the skyrmion size.<sup>14</sup> In this regard, MnSi has excellent prospects to be a good candidate for applied physics.

To confirm the evident skyrmions, diverse measurement tools such as Lorentz transmission electron microscope, magnetic transmission soft X-ray microscope, magnetic force microscope, and small-angle neutron scattering are used.<sup>15-18</sup> Such microscopic tools allow to directly identify the skyrmionic lattice in real-space, but high-quality single crystals or epitaxial thin films are demanded, which are grown by special instruments with high-vacuum chamber. The other way to reveal the existence of skyrmions is considered to measure magnetotransport properties, topological Hall effect (THE), as shown in previous reports.<sup>9,19-21</sup> The skyrmion can be observed even in polycrystalline samples because of being a topological object,<sup>22</sup> in which topological phase is less susceptible to impurities or crystalline nature.

Here, we report the magnetotransport properties of polycrystalline MnSi grown by conventional sputtering. We employed the X-ray diffraction (XRD) and transmission electron microscope (TEM) to identify the single phase of MnSi crystals and their crystallinity. The magnetic transition at around 25 K was revealed by measuring temperature dependent magnetization and resistance curves, where magnetoresistance data also exhibited distinguishable shape at the border of transition temperature. We successfully extracted THE signal from measured Hall resistance, and plotted contour mapping of topological Hall resistivity as a function of temperature and magnetic field. Moreover, the analysis of anomalous Hall resistivity contribution in MnSi films implied the stabilization of the skyrmion phase in a broader range of temperatures and magnetic fields, albeit impurities and defects in polycrystalline MnSi sample. Our finding provides the results that the skyrmions can be observed in polycrystalline MnSi films grown by facile and inexpensive instruments and further investigations of the similar materials possessing skyrmionic lattices can be stimulated.

## Methods

MnSi films were deposited on Si (001) and *c*-cut sapphire ( $\text{Al}_2\text{O}_3$ ) substrates by direct current (DC) / radio frequency (RF) magnetron sputtering with a base pressure of  $1.0 \times 10^{-6}$  Torr. The MnSi films were grown at room temperature under 10 mTorr Ar pressure by co-sputtering Mn and Si target with 5 min. The DC power for Mn target was 10 to 20 W, and the RF power for Si target was 100 W. Following deposition of MnSi, as-grown MnSi was crystallized by inducing in-situ annealing treatment for 2 hours at the temperature range of 550 ~ 590 °C. The crystal phase and structure of the samples were examined by XRD with an X-ray source of Mo and Ag at 60 kV. The morphological characterization and chemical composition of the samples were analyzed by scanning electron microscopy (SEM), atomic force microscopy (AFM), and high-resolution transmission electron microscopy (HR-TEM) equipped with an energy dispersive spectroscopy (EDS). The magnetic and electrical properties were measured using a superconducting quantum interference device-vibrating sample magnetometer (SQUID-VSM), where the magnetic field and temperature were swept up to 50 kOe and down to 2 K, respectively.

## Results And Discussion

The growth of MnSi films have been well described in previous reports with various methods.<sup>2,9,21-25</sup> However, most techniques to grow MnSi required specific facilities with an ultrahigh vacuum environment, while development for conventional magnetron sputtering with relatively low base pressure is not introduced yet. Since the lattice mismatch between Si (001) substrate and cubic MnSi structure is estimated to be around 19%, we have tested to find optimal growth conditions of the MnSi films on Si (001) substrates. Co-sputtering method with Mn and Si targets were employed, and growth conditions such as RF power, growth temperature, and annealing treatments were minutely controlled to grow the MnSi films (Table S1 of the supplementary information). Aguf *et al.* reported that as-deposited MnSi films were amorphous unless they were crystallized by annealing treatment.<sup>23</sup> Indeed, we found that initially deposited amorphous MnSi turned into crystallized MnSi phase after annealing treatment (Fig. S1 of the

supplementary information). Most results using Si (001) substrate, however, showed that mixed phases of MnSi and Mn<sub>5</sub>Si<sub>3</sub> were observed by XRD measurements. For this reason, Si (001) substrates were replaced by Al<sub>2</sub>O<sub>3</sub> substrates having a low lattice mismatch (~ 4.2%).

Fig. 1 presents the XRD patterns of the MnSi films grown on Si (black solid line) and Al<sub>2</sub>O<sub>3</sub> (blue and red solid lines) substrates, where the MnSi films on Si (001) and on Al<sub>2</sub>O<sub>3</sub> #1 were deposited with same growth conditions (15 W for Mn power, 100 W for Si, 590 °C annealing treatment). Note that the substrate peaks were not displayed for all samples because grazing incident X-ray diffraction technique was used. The asterisk in the Figure indicates Mn<sub>5</sub>Si<sub>3</sub> (ICSD card no. 04-003-4114) phase. For the MnSi film on Si (001), MnSi peaks were mainly observed, in addition five peaks matched with Mn<sub>5</sub>Si<sub>3</sub> phase and several unknown impurity peaks were detected. However, we found out that the peaks related with Mn<sub>5</sub>Si<sub>3</sub> phase were suppressed and the unknown peaks disappeared for the MnSi on Al<sub>2</sub>O<sub>3</sub> #1. Furthermore, MnSi on Al<sub>2</sub>O<sub>3</sub> #2 sample, for which Mn power and annealing temperature decreased to 10 W and 550 °C, respectively, showed only MnSi (ICSD card no. 04-004-7568) peaks.

Although as-grown MnSi on Al<sub>2</sub>O<sub>3</sub> #2 showed somewhat defective surface, highly uniform and low uneven surface was observed, as shown in SEM image of Fig. 2a and AFM topographic image of Fig. 2b. In the 15×15 μm scale of AFM image, the root mean squared (RMS) roughness was measured to be under 1 nm. To characterize detailed structure and chemical composition, the cross-sectional TEM analyses of as-grown MnSi on Al<sub>2</sub>O<sub>3</sub> #2 were carried out. Fig. 2c shows the representative cross-sectional TEM image of MnSi on Al<sub>2</sub>O<sub>3</sub> #2 at the interfacial region. Note that no stacking faults nor significant defects were observed. When one grows MnSi films grown by conventional sputtering in a relatively low vacuum chamber, it is hard to expect that MnSi grows epitaxially to the preferred direction of the surface of substrates, considering the structural parameters such as lattice mismatch and chemical bonding. Our MnSi films grown on Al<sub>2</sub>O<sub>3</sub> have polycrystalline nature, confirmed by XRD patterns (Fig. 1) and fast Fourier transform (FFT) of TEM image [inset of Fig. 2c]. We have examined chemical composition of as-grown MnSi films. As seen in TEM-EDS mapping of Fig. 2d, the presence of only Mn and Si elements was detected at several different regions, and the atomic ratio of Mn : Si = 1 : 1.1 is estimated. We tested the growth rate of MnSi films by controlling growth time. The thickness of as-grown MnSi films showed a linear behavior for the growth time (Fig. S2 of the supplementary information).

Fig. 3a shows the temperature dependence of magnetization for MnSi on Al<sub>2</sub>O<sub>3</sub> (thickness; 25 nm) measured in an out-of-plane magnetic field of 1 kOe. The magnetization dropped significantly at temperatures above 25 K, indicating the ferromagnetic transition temperature ( $T_C$ ), similar to the bulk MnSi.<sup>26,27</sup> The resistivity depending on the temperature exhibited metallic behavior above  $T_C$ , as shown in Fig. 3b. Below  $T_C$ , the resistivity tended to decrease with  $T^2$  dependence as decreasing temperatures, owing to the coupling of charge carriers to spin fluctuations in helimagnetic phase.<sup>28</sup> As seen in the inset of Fig. 3b, the derivative of resistivity versus temperature highlighted  $T_C$  of MnSi films, around 25 K. The

polycrystal and defects on the surface give rise to the low residual resistivity ratio,  $[\rho(300\text{ K}) / \rho(5\text{ K})] \sim 1.7$ .

Fig. 3c shows the magnetoresistance for the magnetic fields perpendicular to the film plane at different temperatures of 2 K, 25 K, and 50 K. As we discussed above, since as-grown MnSi films had polycrystalline nature, the magnetic phase transition from the magnetoresistance was not clearly observed. In low magnetic fields, however, the temperature dependence of the magnetoresistance exhibited distinguishable features. As the temperature increased, the shape of the magnetoresistance in the vicinity of zero magnetic field changed from flat (2 K) to sharp (25 K) and broad (50 K) peaks.

Spin-chirality-driven Hall effect, THE can be induced by DMI arising from strong spin-orbit coupling and non-centrosymmetric B20 crystal structure,<sup>29</sup> considered as a hallmark for the existence of skyrmion phase. We have performed Hall resistivity measurement to observe abnormal resistivity related with THE. The total Hall resistivity can be expressed as a combination of three components:

$$\begin{aligned} \rho_{Hall} &= \rho_{normal} + \rho_{AHE} + \rho_{THE} \\ &= R_0 H + (\alpha \rho_{xx0} + \beta \rho_{xx0}^2 + b \rho_{xx}^2) M + n_{Skx} P R_{TH} B_{eff}, \end{aligned}$$

where  $\rho_{normal}$ ,  $\rho_{AHE}$ , and  $\rho_{THE}$  are the normal, anomalous, and topological Hall resistivities, respectively.  $R_0$  is the normal Hall coefficient, and  $\alpha$ ,  $\beta$ , and  $b$  are the constants corresponding to the skew scattering, side jump, and intrinsic contributions to the anomalous Hall resistivity. Also,  $n_{Skx}$  is the relative skyrmion density,  $P$  is the polarization of the conduction electrons,  $R_{TH}$  is the topological Hall coefficient, and  $B_{eff}$  is the effective magnetic field derived from the real-space Berry phase.<sup>20,30</sup> Topological Hall contribution can be extracted by subtracting the normal and anomalous Hall resistivity terms from the measured total Hall resistivity.

Fig. 4a shows deconvoluted Hall data to extract the THE signal at 10 K as the blue curve, including normal (green line) and anomalous (red curve) Hall resistivities. Note that the positive slope of  $\rho_{normal}$  indicates  $p$ -type majority carriers, and  $\rho_{AHE}$  is negative, consistent with those of MnSi bulk,<sup>31</sup> thin film,<sup>9</sup> and nanowire.<sup>20</sup> The  $\rho_{normal}$  is obtained from the linear fit at high magnetic fields, and  $\rho_{AHE}$  is directly taken from the magnetization data. The  $\rho_{THE}$  depending on the temperature is displayed in Fig. 4b. Interestingly, the sign of  $\rho_{THE}$  flipped at the border of 25 K, where the magnetic transition was expected. The sign of  $\rho_{THE}$  is very sensitive to the spin polarization of charge carriers. In the band structure of MnSi, the localized electrons in  $d$  band affect the density of states near Fermi level, while itinerant electrons in  $s$  band are contributed meagerly in band structure,<sup>31</sup> allowing the spin polarization to be delicate. In addition, since the spin polarization can be changed by external factors such as tensile strain and crystal purity with temperature,<sup>9</sup> the flipped sign of  $\rho_{THE}$  in our polycrystalline MnSi sample is reasonable. Fig. 4c

presents the contour mapping of  $\rho_{\text{THE}}$  as a function of magnetic field and temperature. While skyrmion phase in bulk MnSi was observed in narrow temperature range close to the magnetic transition temperature, non-zero  $\rho_{\text{THE}}$  was collected from 2 K to 40 K regardless the sign. The absolute value of  $\rho_{\text{THE}}$  had a maximum of 36 n $\Omega$ .cm at 10 K and 4 kOe, larger than thin films grown by MBE (10 n $\Omega$ .cm),<sup>9</sup> bulk (4.5 n $\Omega$ .cm),<sup>32</sup> and nanowire (15 n $\Omega$ .cm)<sup>20</sup> but similar to the thin films grown by off-axis magnetron sputtering with ultrahigh vacuum chamber.<sup>25</sup>

$\rho_{\text{AHE}}$  consists of three components; skew scattering, side jump, and intrinsic contribution. Implication in the scaling of anomalous Hall contribution is that  $\rho_{\text{AHE}}$  is proportional to the intrinsic contribution, associated with momentum-space Berry phase.<sup>33</sup> In Fig. 4d, we plot the  $\rho_{\text{AHE}}$  against at 20 kOe, showing obvious deviation from linear dependence. The breakdown of the scaling suggests that anomalous Hall effect is relevant to extrinsic skew scattering and side jump contributions caused by impurities and defects in our polycrystalline MnSi sample, remaining the stabilization of the skyrmion phase in a broader range of temperatures and magnetic fields.

## Conclusion

In summary, we demonstrated a method to grow MnSi films on Al<sub>2</sub>O<sub>3</sub> by conventional magnetron sputtering with relatively low vacuum chamber. The spectroscopic and morphological analyses confirmed that as-deposited MnSi films have polycrystalline nature with highly uniform and low rough surface. The transport properties exhibit the intrinsic characteristics of MnSi, though magnetic transition temperature was slightly lower than that of previous results. More importantly, we observe stable skyrmion phase in a broad range of temperatures and magnetic fields even in our polycrystalline MnSi films, attributed to the complicated implication of Hall resistivities contribution. This work opens up the opportunity for extensive investigation on the materials possessing skyrmion phase, beyond the burden to prepare single crystals or epitaxial thin films

## Abbreviations

DMI: Dzyaloshinskii-Moriya interaction; STT: spin transfer torque; THE: topological Hall effect; XRD: X-ray diffraction; TEM: transmission electron microscope; Al<sub>2</sub>O<sub>3</sub>: sapphire; DC: direct current; RF: radio frequency; SEM: scanning electron microscopy; AFM: atomic force microscopy; HR-TEM: high-resolution transmission electron microscopy; EDS: energy dispersive spectroscopy; SQUID-VSM superconducting quantum interference device-vibrating sample magnetometer; RMS: root mean squared; FFT: fast Fourier transform;  $T_C$ : ferromagnetic transition temperature

## Declarations

## Acknowledgements

Not applicable

## Authors' Contributions

S.L. and M.H.J conceived the idea and designed the experiments. W.Y.C. and H.W.B. grew the MnSi thin films on Al<sub>2</sub>O<sub>3</sub> substrate. S.H.C. and S.L. performed spectroscopic and morphological measurements and analyses. W.Y.C., H.W.B. and M.H.J carried out the magnetometric and transport measurements. The manuscript was written by W.Y.C., S.L. and M.H.J. with input from all authors.

## Funding

This work was supported by the National Research Foundation of Korea (NRF) grant funded by the Korea government (MSIT) (Nos. 2016R1E1A1A01942649, 2018R1D1A1B07048109, and 2020R1A2C3008044).

## Availability of Data and Materials

All data generated or analysed during this study are included in this published article and its supplementary information files, and are available from corresponding author on reasonable request.

## Competing Interests

The authors declare that they have no competing interests.

## References

1. U. K. Roszler, A. N. Bogdanov, and C. Pfleiderer, *Nature* **442**, 797 (2006).
2. D. Schroeter, N. Steinki, M. Schilling, A. Fernández Scarioni, P. Krzysteczko, T. Dziomba, H. W. Schumacher, D. Menzel, and S. Süllow, *J. Phys.: Condens. Matter* **20**, 235805 (2018).
3. T. Schulz, R. Ritz, A. Bauer, M. Halder, M. Wagner, C. Franz, C. Pfleiderer, K. Everschor, M. Garst, and A. Rosch, *Nat. Phys.* **8**, 301 (2012).
4. A. Fert, V. Cros, and J. Sampaio, *Nat. Nanotechnol.* **8**, 152 (2013).
5. F. Jonietz, S. Mühlbauer, C. Pfleiderer, A. Neubauer, W. Münzer, A. Bauer, T. Adams, R. Georgii, P. Böni, R. A. Duine, K. Everschor, M. Garst, and A. Rosch, *Science* **330**, 1648 (2010).
6. G. G. Lonzarich and L. Taillefer, *J. Phys. C: Solid State Phys.* **18**, 4339 (1985).
7. E. Magnano, F. Bondino, C. Cepek, F. Parmigiani, and M. C. Mozzati, *Appl. Phys. Lett.* **96**, 152503 (2010).
8. A. Tonomura, X. Z. Yu, K. Yanagisawa, T. Matsuda, Y. Onose, N. Kanazawa, H. S. Park, and Y. Tokura, *Nano Lett.* **12**, 1673 (2012).
9. Y. Li, N. Kanazawa, X. Z. Yu, A. Tsukazaki, M. Kawasaki, M. Ichikawa, X. F. Jin, F. Kagawa, and Y. Tokura, *Phys. Rev. Lett.* **110**, 117202 (2013).

10. S. L. Zhang, R. Chalasani, A. A. Baker, N.-J. Steinke, A. I. Figueroa, A. Kohn, G. van der Laan, and T. Hesjedal, *AIP Adv.* **6**, 015217 (2016).
11. X. Yu, J. P. DeGrave, Y. Hara, T. Hara, S. Jin, and Y. Tokura, *Nano Lett.* **13**, 3755 (2013).
12. A. Bisig, C. A. Akosa, J.-H. Moon, J. Rhensius, C. Moutafis, A. von Bieren, J. Heidler, G. Kiliani, M. Kammerer, M. Curcic, M. Weigand, T. Tyliczszak, B. van Waeyenberge, H. Stoll, G. Schutz, K.-J. Lee, A. Manchon, and M. Kläui, *Phys. Rev. Lett.* **117**, 277203 (2016).
13. P. B. Ndiaye, C. A. Akosa, and A. Manchon, *Phys. Rev. B* **95**, 064426 (2017).
14. X. S. Wang, H. Y. Yuan, and X. R. Wang, *Commun. Phys.* **1**, 31 (2018).
15. X. Z. Yu, N. Kanazawa, W. Z. Zhang, T. Nagai, T. Hara, K. Kimoto, Y. Matsui, Y. Onose, and Y. Tokura, *Nat. Commun.* **3**, 988 (2012).
16. S. Woo, K. M. Song, H.-S. Han, M.-S. Jung, M.-Y. Im, K.-S. Lee, K. S. Song, P. Fischer, J.-I. Hong, J. W. Choi, B.-C. Min, H. C. Koo, and J. Chang, *Nat. Commun.* **8**, 15573 (@017).
17. P. Milde, D. Köhler, J. Seidel, L. M. Eng, A. Bauer, A. Chacon, J. Kindervater, S. Mühlbauer, C. Pfleiderer, S. Buhandt, C. Schütte, and A. Rosch, *Science* **340**, 1076 (2018).
18. T. Nakajima, H. Oike, A. Kikkawa, E. P. Gilbert, N. Booth, K. Kakurai, Y. Taguchi, Y. Tokura, F. Kagawa, and T. Arima, *Sci. Adv.* **3**, e1602562 (2017).
19. H. Du, J. P. Degrave, F. Xue, D. Liang, W. Ning, J. Yang, M. Tian, Y. Zhang, and S. Jin, *Nano Lett.* **14**, 2026 (2014).
20. D. Liang, J. P. DeGrave, M. J. Stolt, Y. Tokura, and S. Jin, *Nat. Commun.* **6**, 8217 (2015).
21. D. Menzel, D. Schroeter, N. Steinki, S. Süllow, A. Fernández Scarioni, H. W. Schumacher, H. Okuyama, H. Hidaka, and H. Amitsuka, *IEEE Trans. Magn.* **55**, 1500204 (2019).
22. F. Qian, J. Feng, J. Fan, L. Ling, Y. Ji, Y. Liu, Y. Shi, X. Miao, D. Shi, and H. Yang, *Mater. Lett.* **257**, 126714 (2019).
23. V. Aguf, J. Pelleg, and M. Sinder, *AIP Adv.* **5**, 067124 (2015).
24. M. N. Wilson, E. A. Karhu, A. S. Quigley, U. K. Rößler, A. B. Butenko, A. N. Bogdanov, M. D. Robertson, and T. L. Monchesky, *Phys. Rev. B* **86**, 144420 (2012).
25. J. López-López, J. M. Gomez-Perez, A. Álvarez, H. B. Vasili, A. C. Komarek, L. E. Hueso, F. Casanova, and S. Blanco-Canosa, *Phys. Rev. B* **99**, 144427 (2019).
26. S. Mühlbauer, B. Binz, F. Jonietz, C. Pfleiderer, A. Rosch, A. Neubauer, R. Georgii, and P. Boni, *Science* **323**, 915 (2009).
27. E. Karhu, S. Kahwaji, T. L. Monchesky, C. Parsons, M. D. Robertson, and C. Maunders, *Phys. Rev. B* **82**, 184417 (2010).
28. T. Moriya, *Spin fluctuations in itinerant electron magnetism*, 1st ed. (Springer series in solid-state science, New York: Springer, 1985).
29. M. Leroux, M. J. Stolt, S. Jin, D. V. Pete, C. Reichhardt, and B. Maiorov, *Sci. Rep.* **8**, 15510 (2018).
30. N. Nagaosa, J. Sinova, S. Onoda, A. H. MacDonald, and N. P. Ong, *Rev. Mod. Phys.* **82**, 1539 (2010).

31. M. Lee, W. Kang, Y. Onose, Y. Tokura, and N. P. Ong, Phys. Rev. Lett. **102**, 186601 (2009).
32. A. Neubauer, C. Pfleiderer, B. Binz, A. Rosch, R. Ritz, P. G. Niklowitz, and P. Böni, Phys. Rev. Lett. **102**, 186602 (2009).
33. D. Hou, G. Su, Y. Tian, X. Jin, S. A. Yang, and Q. Niu, Phys. Rev. Lett. **114**, 217203 (2015).

## Figures

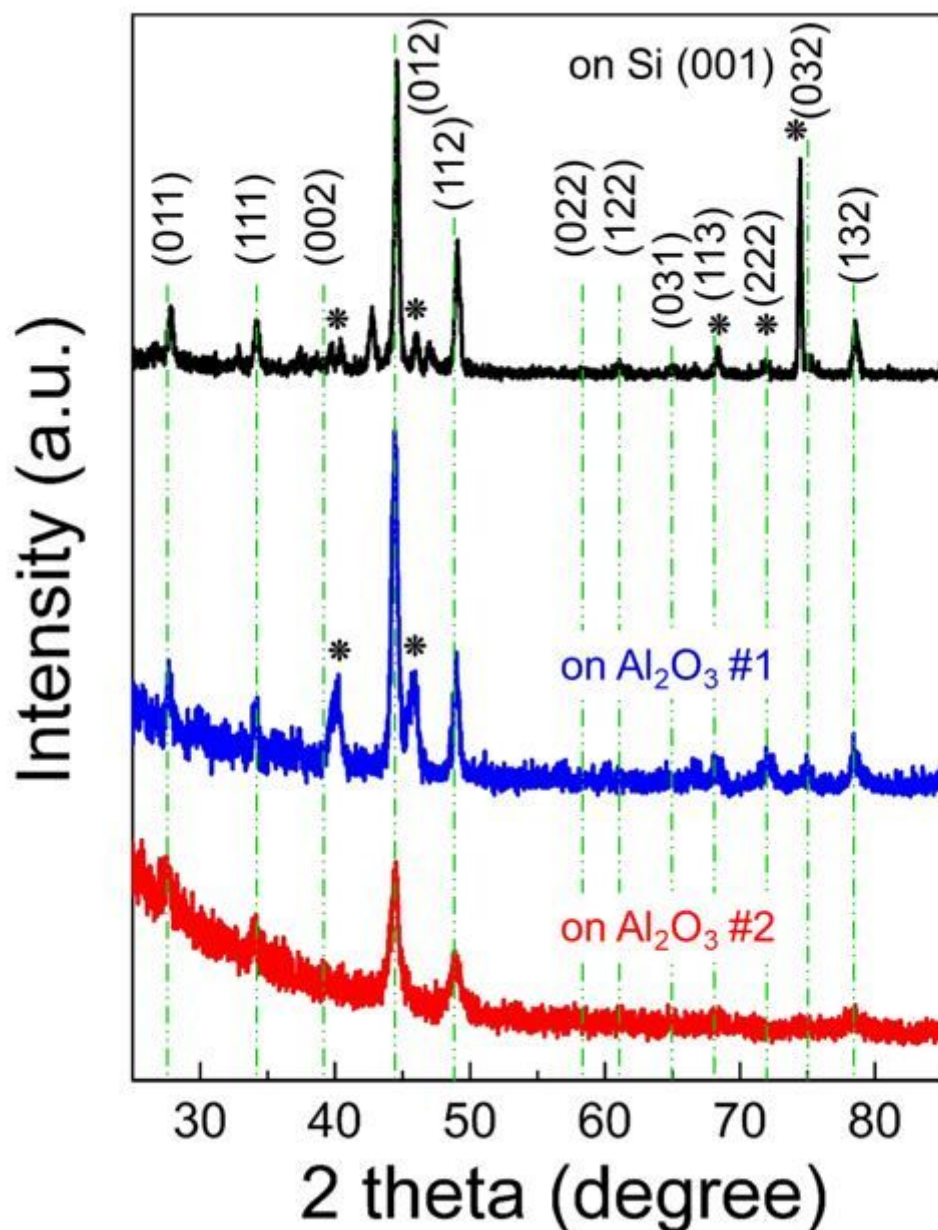
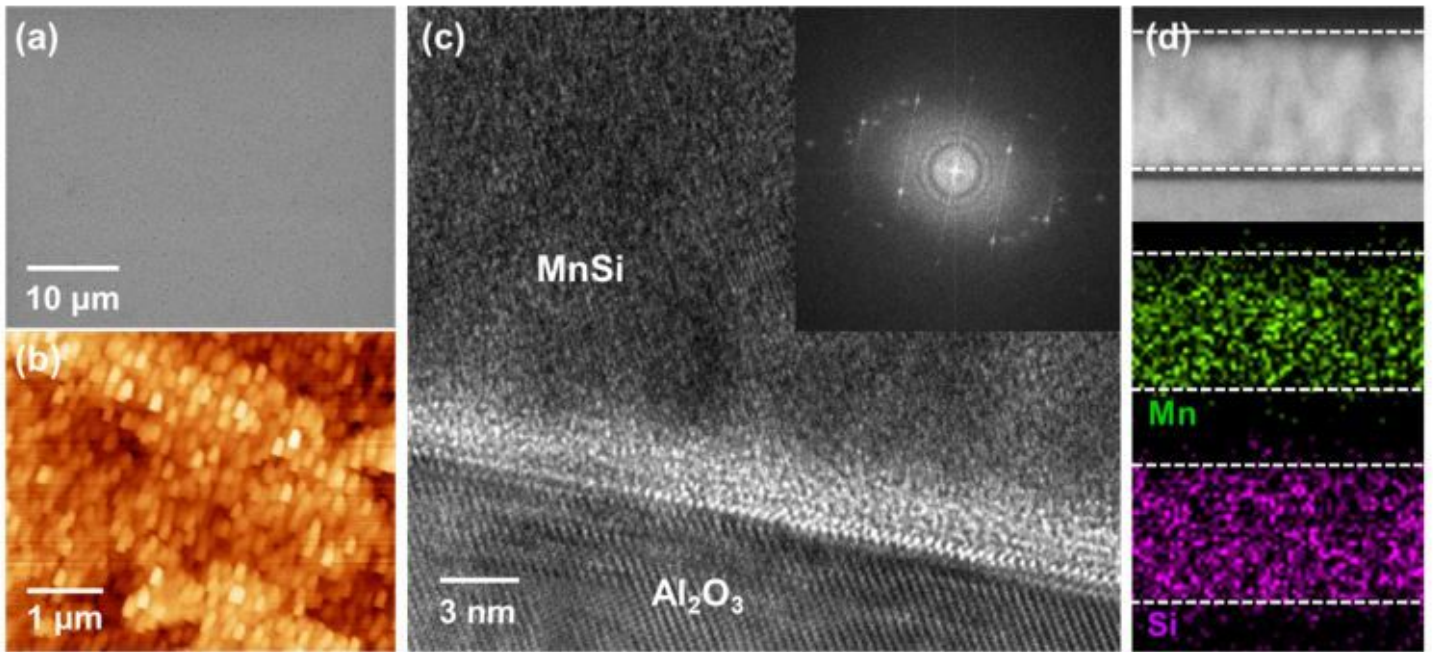


Figure 1

XRD pattern of MnSi films on Si [(001), black solid line] and Al<sub>2</sub>O<sub>3</sub> (blue and red solid lines) substrate. All the peaks are indexed to the cubic B20-type MnSi phase, marked with green dotted lines. The asterisks in black and blue solid lines indicate the peaks from Mn<sub>5</sub>Si<sub>3</sub> phase.



**Figure 2**

Morphological and structural characterization of MnSi film grown on Al<sub>2</sub>O<sub>3</sub> substrate. (a) SEM image of the as-grown MnSi film. (b) AFM topographic image corresponding to Figure 2(a). RMS roughness is estimated to be under 1 nm. (c) Representative HR-TEM image of MnSi film grown on sapphire. Inset: FFT from selected area of MnSi in HR-TEM image. (d) Elemental mapping of the EDS of the cross-sectional MnSi film.

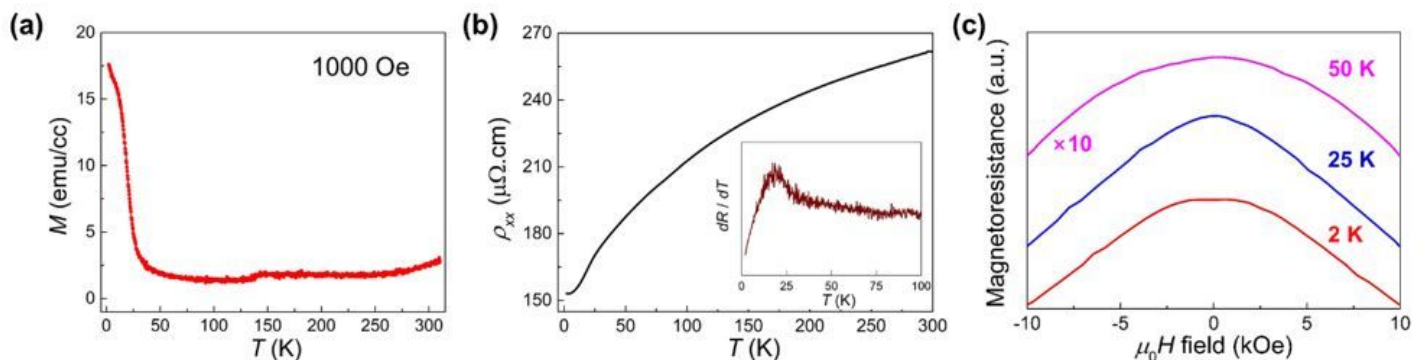


**Figure 3**

(a) Field-cooled magnetization as a function of temperature for 25 nm thick MnSi film in an external magnetic field of 1 kOe. (b) Zero-field longitudinal resistance as a function of temperature. Inset: derivative of the resistance vs temperature highlighting the anomaly of magnetic transition. (c) Perpendicular magnetoresistance at 2, 25, and 50 K. For clarity, the arbitrary offsets are added, and the magnetoresistance measured at 50 K is magnified by 10 times.

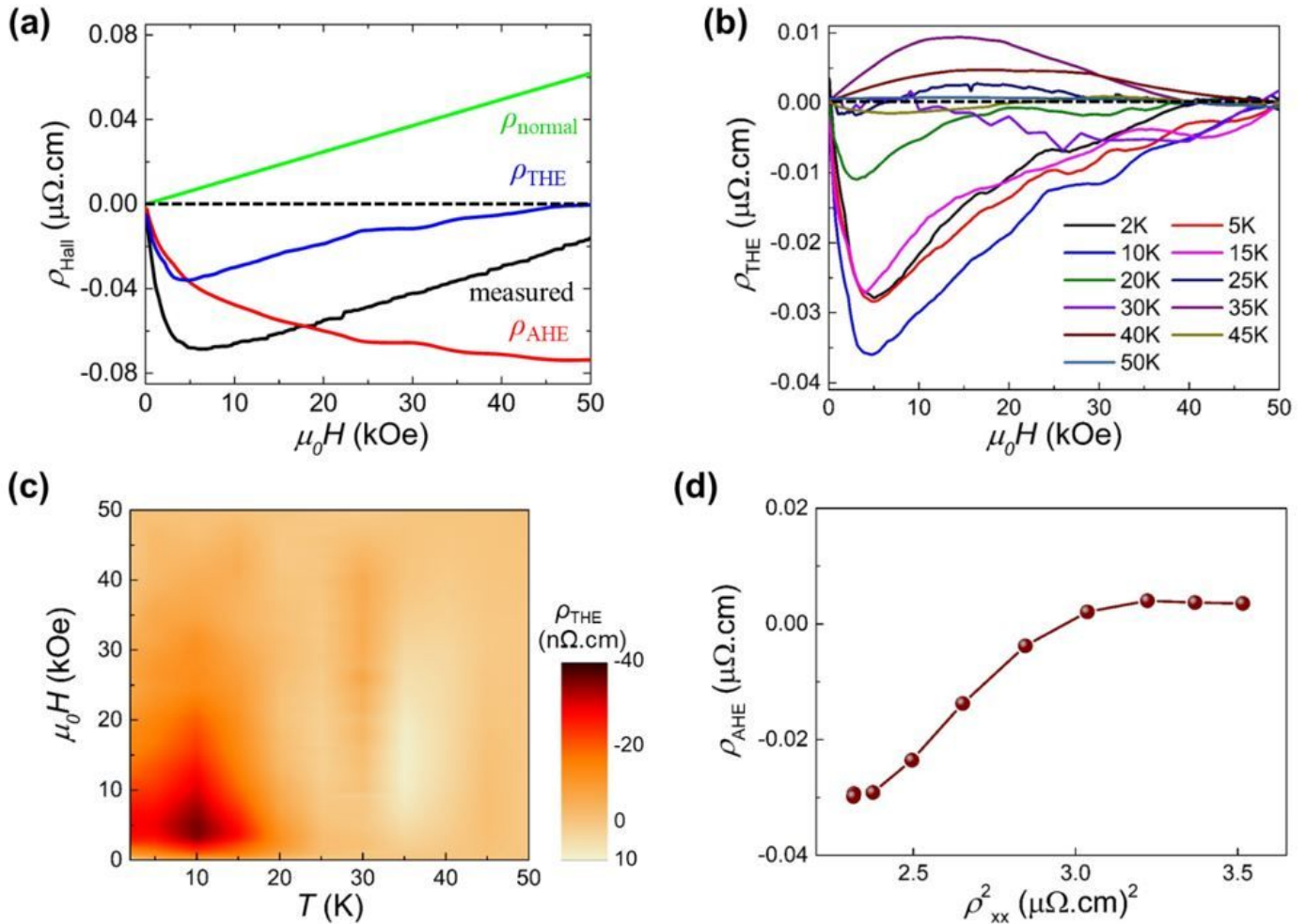


**Figure 4**

(a) The representative Hall resistivity curve at 10 K. THE signal (blue curve) is extracted by subtracting normal (green line) and anomalous Hall signal (red curve) from total measured Hall resistivity (black curve). (b) topological Hall resistivities at various temperatures, extracted using the same procedure detailed in the text. (c) The contour mapping of THE signal as a function of the magnetic field and temperature, constructed by interpolation of topological Hall resistivity between temperatures. (d) Anomalous Hall resistivity as a function of squared longitudinal magnetoresistivity below the temperature, where topological Hall resistivity is not zero.

## Supplementary Files

This is a list of supplementary files associated with this preprint. Click to download.

- [suppinfnanoscaleres.lett..docx](#)